Pulse-induced crystallization in phase change memories under set and disturb conditions

Nicola Ciocchini, *Student Member, IEEE*, and Daniele Ielmini, *Senior Member, IEEE*

I. Introduction

Phase change memory (PCM) is today regarded as one of the main candidates for future non-volatile memory (NVM) [1], thanks to fast switching [2], scalable programming power [3] and industrial maturity [4]. Crystallization processes in the PCM control set transition [5], data retention [6] and program/read disturb effects [7], [8]. In fact, programming to the low-resistance (set) state is achieved by application of a voltage pulse inducing Joule-heating and consequent crystallization of the amorphous phase [9]. Similarly, Joule heating during read [8] or during programming of a neighboring cell in the array [10] may lead to undesired crystallization and consequent degradation of the resistance. On the other hand, the temperature-dependent data retention of the high-resistance (reset) state is dictated by the spontaneous crystallization of the amorphous phase.

In this work, we propose a comprehensive study of crystallization kinetics in PCM devices. To this purpose, we introduce a new technique to extend the study of crystallization to extremely low currents (above 20 μA) in the set regime. To further extend the current and time range of the measurement, we perform crystallization experiments in the sub-threshold regime which is relevant for read disturb evaluations. Finally, we develop a finite element model to predict the time evolution of the chalcogenide phase (hence resistance) upon crystallization. The new model is able to account for crystallization time in a wide range of currents in both set and read disturb regimes.

Preliminary results of this work were previously reported [11]. With respect to this previous work, we extend the description of the finite element model and of the simulation results, highlighting the impact of the programming current on the set characteristics and the self-limiting evolution of the resistance during disturb in the subthreshold regime.

N. Ciocchini and D. Ielmini are with the Dipartimento di Elettronica, Informazione e Bioingegneria and Italian Universities Nanoelectronics Team (IU.NET), Politecnico di Milano, piazza L. da Vinci 32, 20133 Milano, Italy. E-mail: daniele.ielmini@polimi.it

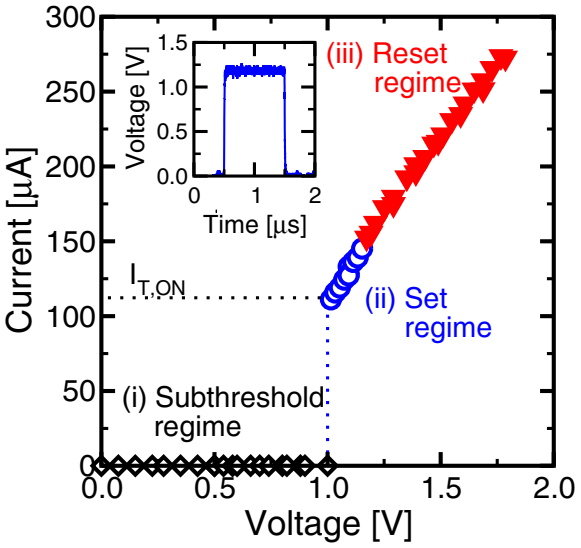

Fig. 1. Measured I-V curves of a 45 nm PCM device. Data were obtained with a single pulse approach (inset). Three current regimes are highlighted: (i) subthreshold regime, (ii) set regime and (iii) reset regime. Note that the single pulse approach limits the current in the set regime to $I_{T,ON}$.

II. Set regime

Fig. 1 shows a typical I-V curve for a PCM device in a 45 nm technology [4]. The I-V curve was obtained by applying several voltage pulses with different amplitude to the cell. We measured the current in response to the applied pulse as the voltage across a 50 Ω resistor in series to the PCM cell. The measured I-V characteristic displays three different current regimes, namely: subthreshold regime ($I < 10$ μA), which is the region explored during the read operation, set regime (10 μA $< I <$ 150 μA), where Joule-heating induces crystallization of the amorphous phase, and reset regime ($I > 150$ μA) where Joule heating induces reset transition by melting and quenching mechanisms.

The differential resistance $R_{ON} \approx 5$ kΩ in the ON regime of Fig. 1 is dominated by the resistance of the thin bottom electrode contact, since the resistivity of amorphous GST is lowered by orders of magnitude after threshold switching [5].

Threshold voltage $V_T \approx 1$ V usually limits the study of set kinetics to a confined current range above $I_{T,ON} = 110$ μA in Fig. 1. The commonly employed method to avoid this limitation consists in adding a resistive element in series with the PCM device, such as (i) a load resistance R_L or (ii) an

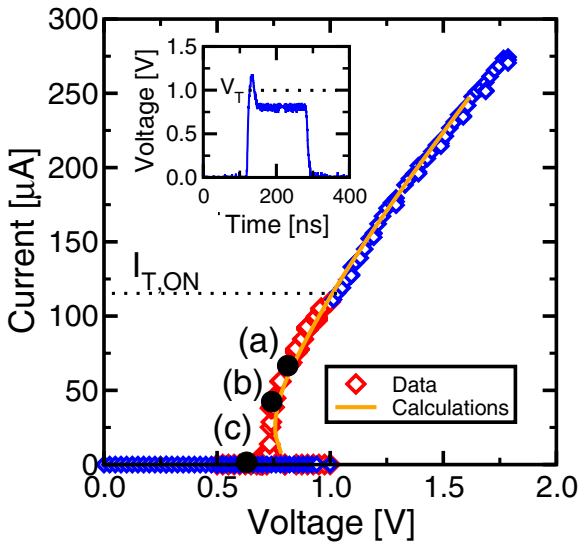

Fig. 2. Measured I-V curve using the modulated-pulse technique (inset), allowing to explore the current range $I < I_{T,ON}$ which could not be accessed in Fig. 1. The first short pulse at $V > V_T$ induces threshold switching with negligible crystallization, while the second pulse at $V_{cryst} < V_T$ induces the crystallization of the amorphous phase.

integrated MOSFET device working in the saturated regime. However, oscillations may arise at low I [12], while the presence of a resistance or a transistor capable of limiting the current is not always available in the circuit, *e.g.*, see the case of a select diode in crossbar applications [13]. To overcome this limitations in accessing the ON state at $I < I_{T,ON}$, we propose the modulated-pulse technique shown in the inset of Fig. 2: The first part of the pulse at $V > V_T$ induces threshold switching with negligible crystallization due to the short pulse-width, nominally of 20 ns, but shorter due to impact of RC delays. The second part of the pulse at $V_{cryst} < V_T$ then follows, allowing the set transition at $I < I_{T,ON}$ as shown in Fig. 2. Fig. 3 shows the measured current $I(t)$ during the modulated-pulse waveform with increasing $V_{cryst} < V_T$ (Fig. 3(d)). We can divide the typical current response to the modulated-pulse into 3 categories, namely:

(a) for relatively high V_{cryst} (Fig. 3(a)), the current I_{ON} during the crystallizing pulse is stable, thus allowing to capture the I-V curve as in Fig. 2;

(b) as V_{cryst} approaches the holding voltage $V_H \approx 0.75$ V, the current decays from I_{ON} to the subthreshold state (Fig. 3(b)) in a time t_{ON}, which is randomly distributed and shorter than the duration of the voltage pulse;

(c) for $V_{cryst} < V_H$, the on-state cannot be sustained, thus the current immediately decays to OFF state as the voltage switches to V_{cryst} (Fig. 3(c)). For cases (b) and (c), the abrupt decay of the current to the OFF state can be ascribed to the voltage V_{cryst} being insufficient to sustain the ON state with high conductivity [14]. This technique allows a deeper insight into set kinetics, allowing to monitor phase change across a larger range of currents.

To monitor crystallization kinetics at $I < I_{T,ON}$, the resistance R was measured after the application of the modulated-pulse as in Fig. 3. Fig. 4 shows the resistance R in color scale, where dark and light colors correspond to high and

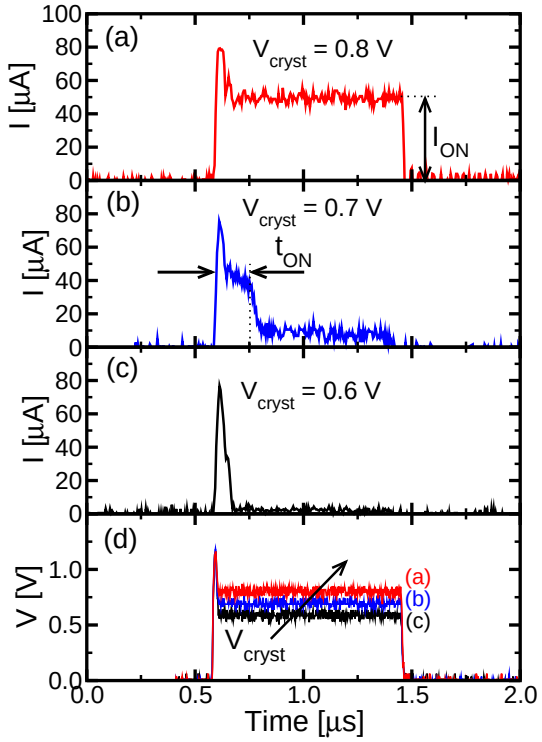

Fig. 3. Measured current response for the modulated pulse technique for $V_{cryst} = 0.8$ V $> V_H$ (a), for $V_{cryst} = 0.7$ V $\approx V_H$ (b) and for $V_{cryst} = 0.6$ V $< V_H$ (c), and the corresponding waveform of the modulated pulse for the 3 cases (d). The PCM remains in the ON state for the whole crystallizing pulse in (a), and only for a random time t_{ON} in (b).

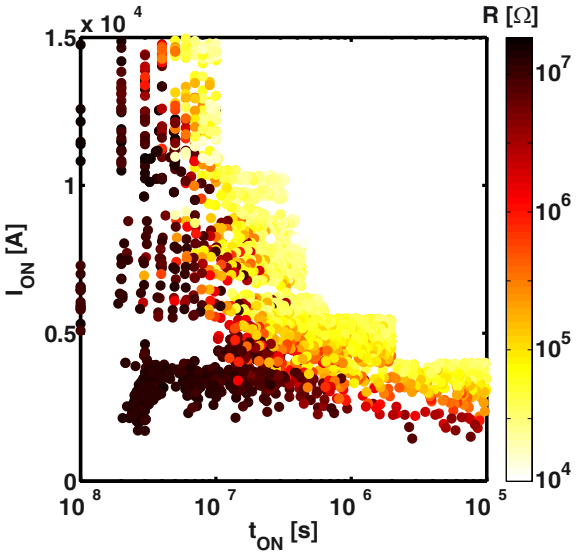

Fig. 4. Measured R in color-scale (light/dark are for low and high R, respectively) as a function of t_{ON} (x-axis) and I_{ON} (y-axis), which are defined in Fig. 3.

low R, respectively, as a function of t_{ON} (x-axis) and I_{ON} (y axis). The time t_{ON} was defined as the length of the crystallizing pulse for case (a) in Fig. 3, and the time for which the device remained in the ON state for case (b) in Fig. 3. Data for case (c) in Fig. 3 are not reported, since no

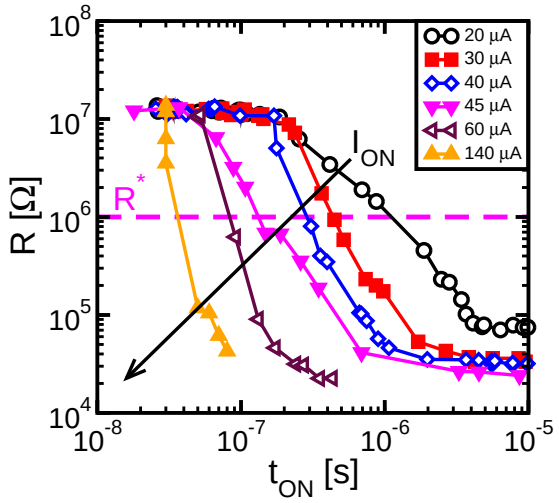

Fig. 5. Measured R as a function of t_{ON} at increasing I_{ON}. Data were obtained by averaging data around a given I_{ON} in Fig. 4. The R behavior indicates 3 regimes, including an initial plateau, a resistance decrease due to localized crystallization and a final saturation regime.

change of R was detected in this case. Before the application of the modulated-pulse, the PCM was always prepared in the amorphous phase with a resistance $R \approx 20$ MΩ by a reset pulse with $V = 1.75$ V and a width of 100 ns. Data in Fig. 4 allow visualizing the crystallization (light colors) area where t_{ON} for the onset of crystallization strongly increases at decreasing I_{ON}. With respect to the standard approach, this technique extends the range of crystallization time to the range of several μs. Crystallization time increases from about 30 ns at $I_{ON} = 100$ μA to about 5 μs at 20 μA.

Fig. 5 shows R as a function of t_{ON}, taken from Fig. 4 by averaging data around a given I_{ON}. The crystallization time t_x, defined as the time for R to decay below $R^* = 1$ MΩ, decreases at increasing I_{ON}, since larger dissipated power induces more Joule heat. Finally, note that the R is not affected by crystallization at $t_{ON} = 20$ ns, even for current above 100 μA. This confirms that the first part of the modulated-pulse cannot affect the crystallization of the PCM. The time-evolution of resistance $R(t)$ can be divided into three distinct regimes: For relatively short times, R remains almost unchanged, since phase change has yet to start in the amorphous chalcogenide. Then R decreases as a consequence of crystallization on a localized path [5] and finally saturates to a value R_{sat}, which depends on the value of the set current I_{ON}. In fact, the measured R_{sat} reported in Fig. 6(a) as a function of I_{ON} shows that data align on the curve $R_{sat} \propto I_{ON}^{-1}$. This behavior can be interpreted by considering the filamentary nature of crystallization in PCM [5], where the effective diameter of the crystallized filament increases with the applied current. Finally, Fig. 6(b) summarizes the measured t_X as a function of I_{ON}, compared with data for 90 nm PCM devices [5]. Note that set current scales down with the technology node basically for two reasons: The first is the different threshold resistance R^* used in the two experiments (1 MΩ and 10 kΩ for the 45 nm and 90 nm devices respectively), while the second is related to the increased thermal resistance of the heater in the scaled technology, resulting in a 2-factor reduction of the

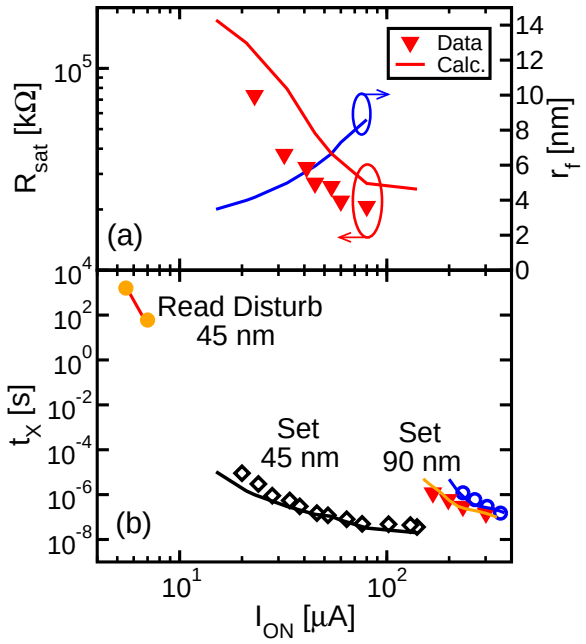

Fig. 6. Measured and calculated R_{sat} as a function of I_{ON} and calculated filament radius r_f according to our filamentary threshold switching model (a), and measured and calculated t_x as a function of I_{ON} (b). R_{sat} decreases with I_{ON} as a result of the increasing filament radius. The crystallization time decreases with I_{ON} due to the increasing Joule heating.

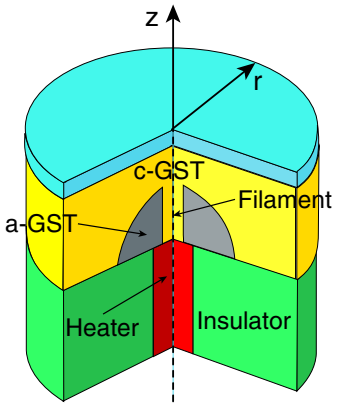

Fig. 7. Schematic of the simulated PCM structure, including an amorphous a cap-shaped amorphous volume with a highly-conductive filament formed by threshold switching.

melting and set currents [4].

III. Modeling Crystallization

To model crystallization in the PCM device, we adopted the Joule-heating numerical model of [5], which was extended to predict the time-evolution of R upon crystallization in Fig. 5. To achieve a reasonable computation time, we reduced the wall structure of the actual device [4] to the 2D axial symmetric PCM device in Fig. 7 [5], [16], [17]. The implemented mushroom-type PCM consists of a GST film enclosed between a W top electrode and a confined TiN bottom electrode (heater). The heater diameter must be interpreted as an effective value which allows reproducing the same electro-thermal behavior of the real device. The transition from a semi-

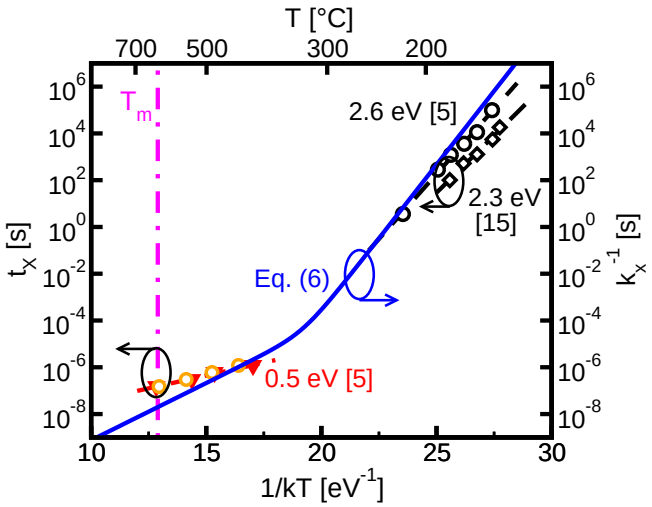

Fig. 8. Measured t_x as a function of $1/kT$ for the thermal regime and the set regime [5]. Data show lower E_x for the set regime, thus evidencing non-Arrhenius crystallization in PCM. PCM data are compared with thermal annealing data for mushroom cells [5], [15]. The inverse of the kinetic constant k_x computed by (6) is also shown (right y-axis).

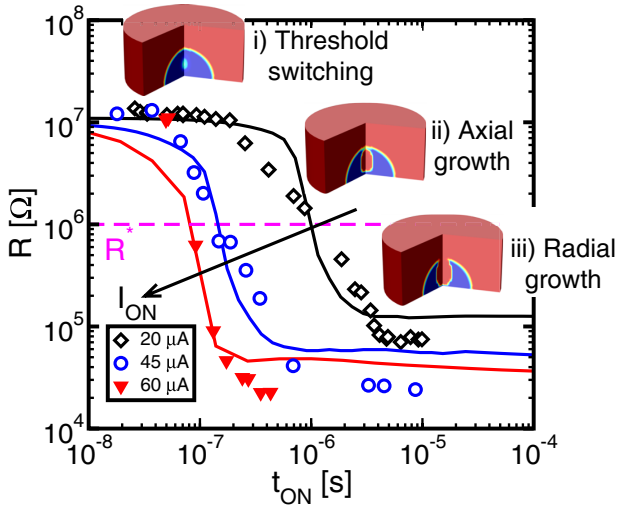

Fig. 9. Measured and calculated R as a function of t_{ON} for increasing $I_{ON} = 20$ μA, 45 μA and 60 μA. The set characteristics evidence 3 regimes: (i) an initial plateau where crystallization does not take place although in the ON state, (ii) a resistance decay due to axial growth of a crystalline path and (iii) an apparent saturation of resistance, due to slow radial growth of the crystalline filament. The insets show calculated f_x for the 3 regimes.

cylindrical to a semi-spherical amorphous dome does not affect our results, since the filament concept is intrinsically area-independent. In addition, the electrical and thermal transport mostly takes place along the z-direction where the electrostatic potential and the temperature display the strongest gradient, which is minimally affected by the change of cell geometry. To compute the electrical current density J, we solved the continuity equation:

$$\nabla J = \nabla(\sigma F) = 0, \tag{1}$$

where we have considered only the drift component of J, that is expressed by the product of the electrical conductivity σ and the electric field F. Equation (1) is solved self-consistently

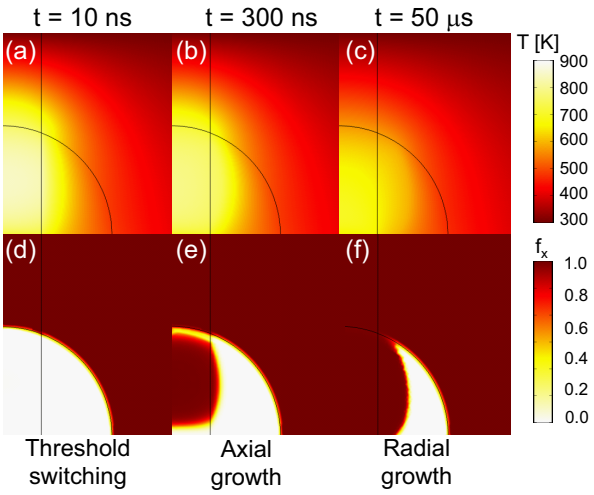

Fig. 10. Calculated T during a set pulse with $I_{ON} = 60$ μA at increasing times, namely $t_{ON} = 10$ ns (a), 300 ns (b) and 50 μs (c), and calculated f_x for the same conditions (d-f). At short times, Joule heating is seen along current path induced by threshold switching (a), although the short time does not allow a phase change (d). At longer times, heating (b) leads to crystallization along the current path (e). Finally, the filament grows in the radial direction (f), causing a decrease of the temperature profile in the amorphous GST (f).

with the heat equation:

$$\nabla(k_{th}\nabla T) + JF = 0, \tag{2}$$

where k_{th} is the thermal conductivity. The first term represents the Fourier heat transport contribution, while the second is the Joule-heating power density. In the model, we took into account the temperature dependence of the GST electrical and thermal conductivities [18], [19].

To describe the phase composition of the GST layer, we introduced a local crystalline fraction f_x ($0 < f_x < 1$). The crystalline fraction allows estimating the electrical conductivity of the mixed phase as:

$$\sigma = f_x\sigma_c + (1 - f_x)\sigma_a, \tag{3}$$

and the thermal conductivity as:

$$k_{th} = f_x k_{th,c} + (1 - f_x)k_{th,a}, \tag{4}$$

where $k_{th,c}$ and $k_{th,a}$ are the thermal conductivities of the crystalline and amorphous phases, respectively. In our model, the crystalline and amorphous phases contribute in parallel to the electrical and thermal conduction for each point of the mesh. We computed the time-evolution of f_x by the rate equation [20]:

$$\frac{df_x}{dt} = -(1 - f_x)k_x, \tag{5}$$

where the thermally-activated crystallization is described by the kinetic constant k_x, which shows a temperature dependence according to:

$$k_x = \left(t_{x1}e^{\frac{E_{x1}}{k_BT}} + t_{x2}e^{\frac{E_{x2}}{k_BT}}\right)^{-1}. \tag{6}$$

Equation (6) is able to reproduce the fragile nature of amorphous GST [21], at the basis of non-Arrhenius set transition [5]. In fact, the kinetic constant k_x is written as the inverse of the sum of two time constants with different pre-exponential

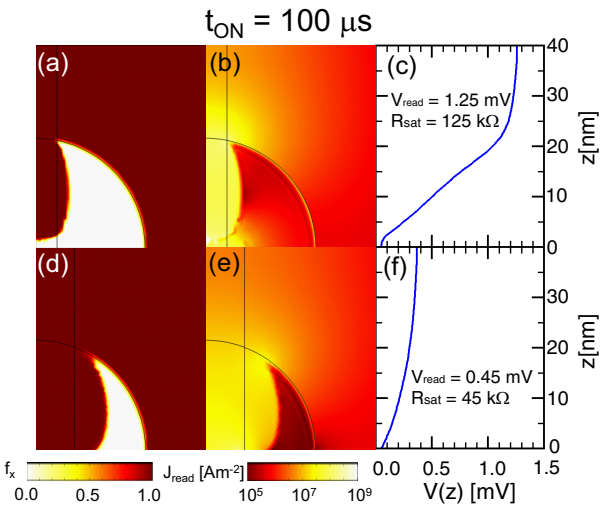

Fig. 11. Color map of calculated f_x (a) and of the calculated read current density J_{read} (b) and corresponding voltage profile along the symmetry axis (c) for $I_{ON} = 20$ μA, and similar results for $I_{ON} = 60$ μA (d-f). The read current was set to $I_{read} = 10$ nA, after a set pulse with $t_{ON} = 100$ μs. A larger I_{ON} results in a larger filament, causing a broader current distribution during read operation and a lower V_{read} at a fixed I_{read}.

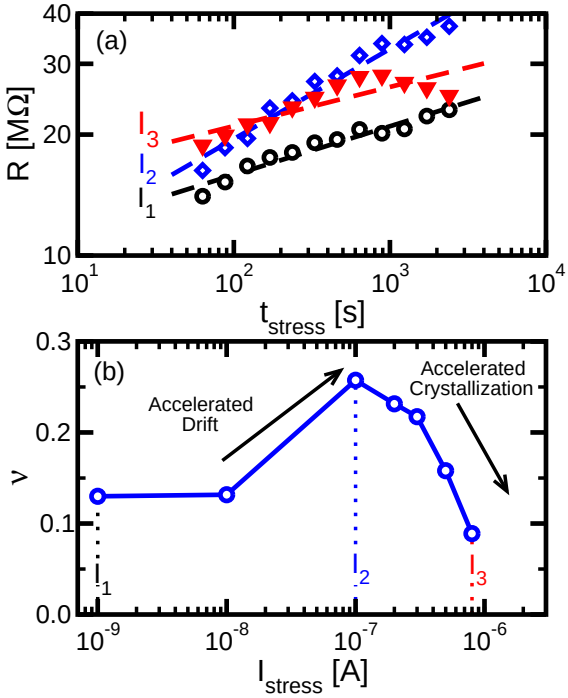

Fig. 12. Measured R as a function of time under CCS at increasing current, namely $I_1 = 1$ nA, $I_2 = 100$ nA and $I_3 = 800$ nA (a) and drift exponent as a function of I_{stress} obtained by fitting R with the power law of (8)(b). Data show an increase of ν with I_{stress}, followed by a decrease of ν due to the onset of crystallization.

factors, namely $t_{x1} = 1.5 \times 10^{-29}$ s and $t_{x2} = 10^{-14}$ s, and the activation energies $E_{x1} = 2.9$ eV and $E_{x2} = 1.1$ eV. The first term controls crystallization at low temperatures below 300°C which are typical of read disturb and thermal annealing regimes, while the second time constant controls crystallization for temperatures above 300°C typical of the set regime, as shown in Fig. 8.

In our model, the current in the reset state flows along a localized channel due to threshold switching, thus causing filamentary crystallization [5]. The filament radius was assumed to increase with current according to:

$$r_f = r_{f0} + \alpha I, \tag{7}$$

where $r_{f0} = 2.2$ nm and $\alpha = 0.088$ nmμA^{-1}. This empirical formula allows reproducing the measured $I-V$ characteristics after threshold switching as shown in Fig. 2.

Fig. 9 shows measured and calculated R for set transition ($t \leq 100$ μs) at 3 increasing levels, namely $I_{ON} = 20$ μA, 45 μA and 60 μA. To obtain the calculated $R - t_{ON}$ curves, we periodically stopped the simulation to allow for low-field read operation at $I_{read} = 10$ nA.

The model accounts for set characteristics in Fig. 9, reproducing the 3 regimes of R behavior, namely the regime at constant R, the resistance decrease and the final saturation. The model also accounts for the decrease of the crystallization time t_x with I_{ON}, as shown by calculations in Fig. 6(b). In particular, the relatively flat $t_x - I_{ON}$ curve at high I_{ON} is captured by our model thanks to the non-Arrhenius crystallization kinetics in (6).

The different regimes in the set characteristics of Fig. 9 are explained as a sequence of (i) threshold switching with no phase-switching, (ii) axial growth and (iii) radial growth of a crystalline filament inside amorphous GST (see the inset in Fig. 9). To better understand this behavior, Fig. 10 shows the calculated T during set transition with $I_{ON} = 60$ μA for increasing set times, namely $t_{ON} = 10$ ns (a), 300 ns (b) and 50 μs (c). At longer times, the relatively high T in the switching filament (b) leads to the axial growth of a crystalline path (e), which dramatically decreases the resistance of the cell in Fig. 9. After completing the axial growth of the filament, crystallization proceeds radially (f) with slower rate due to the lower T in the remaining amorphous phase. In addition, T decreases as a result of the higher content of crystalline phase with a higher thermal conductivity compared to the amorphous phase.

To better understand the relationship between R_{sat} and I_{ON} in Fig. 6(a), Fig. 11 shows the calculated maps of f_x (a) after a set pulse at $I_{ON} = 20$ μA, and the current density J (b) during read at I_{read}. Fig. 11(c) shows the potential profile along the symmetry axis in the chalcogenide layer during read. The set pulse width was 100 μs, which is sufficient to complete the filament growth in the z-direction. Fig. 11(d)-(f) shows similar results but for a larger $I_{ON} = 60$ μA. The higher I_{ON} results in a larger filament according to (7), thus causing a larger crystalline filament after the 100 μs-set pulse. As a result, I_{read} distributes over a larger area in Fig. 11(e), which corresponds to a lower voltage drop in Fig. 11(f).

IV. Read Disturb Regime

Previous studies indicate that Joule heating can take place also in the subthreshold regime, due to the relatively large voltage drop across the amorphous region [22]. To study the effect of electrical stimuli in the subthreshold regime of amorphous GST, Fig. 12(a) shows the resistance R measured during constant current stress (CCS) experiments below threshold

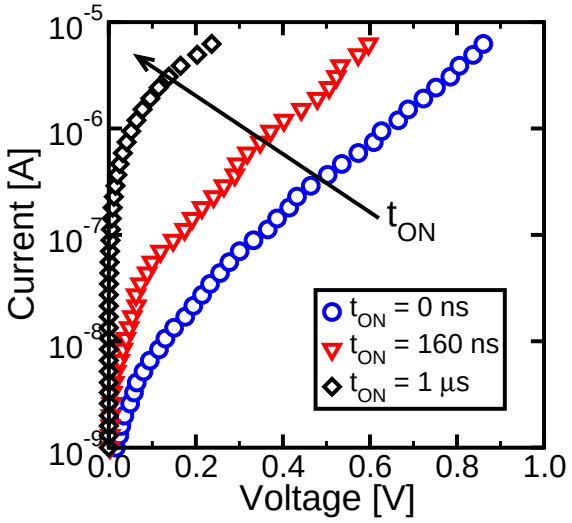

Fig. 13. Measured I-V curve in the subthreshold regime for a PCM in partial set states at increasing t_{ON} = 0 ns, 160 ns and 1 μs in the modulated-pulse technique.

switching, at increasing stress current I_{stress} = 1 nA, 100 nA and 800 nA. To avoid the underestimation of drift at I_{read} > 10 nA highlighted in [23], the resistance was measured at low field, hence low read current (I_{read} = 1 nA). For low $I_{stress} \leq$ 10 nA, only drift is observed in the considered time range, according to the power law [24]:

$$R = R_0 \left(\frac{t}{t_0}\right)^{\nu}, \tag{8}$$

with $\nu \approx 0.12$ being the typical drift exponent. Stressing at I_{stress} = 100 nA causes accelerated drift with higher $\nu \approx 0.25$, due to temperature acceleration [22] or field acceleration [25] of structural relaxation.

At even higher I_{stress} = 800 nA, the R first increases due to drift and the following crystallization at $t > 10^3$ s takes place resulting in R decay. The drift/crystallization effects are summarized in Fig. 12(b), showing the drift coefficient ν extracted over the whole time interval in Fig. 12(a) as a function of I_{stress}. The accelerated drift causes ν increase, then ν decreases due to crystallization along the percolation path [26].

To gain more insight into the crystallization in the subthreshold regime, we conducted CCS experiments on partial set states. Partial set states were obtained by the modulated-pulse technique with variable t_{ON} and I_{ON} = 50 μA, to provide a preferential path for Joule-heating and crystallization. Fig. 13 shows the measured I-V curves for reset, partial set and full set states, showing higher leakage in the partial set state due to the presence of a crystalline channel. The partial set states in the following experiments have resistance in the range between 2 and 8 MΩ and were obtained with t_{ON} below 1 μs.

Fig. 14 shows the measured and calculated R as a function of time during CCS for I_{stress} = 1 μA (a), 5.5 μA (b) and 7 μA (c). Note that the considered stress currents are much higher than the read current for the reset state, which is generally below 100 nA. To ensure a strong immunity of PCM against read disturb during normal memory operation, we took into account the intrinsic variability of crystallization

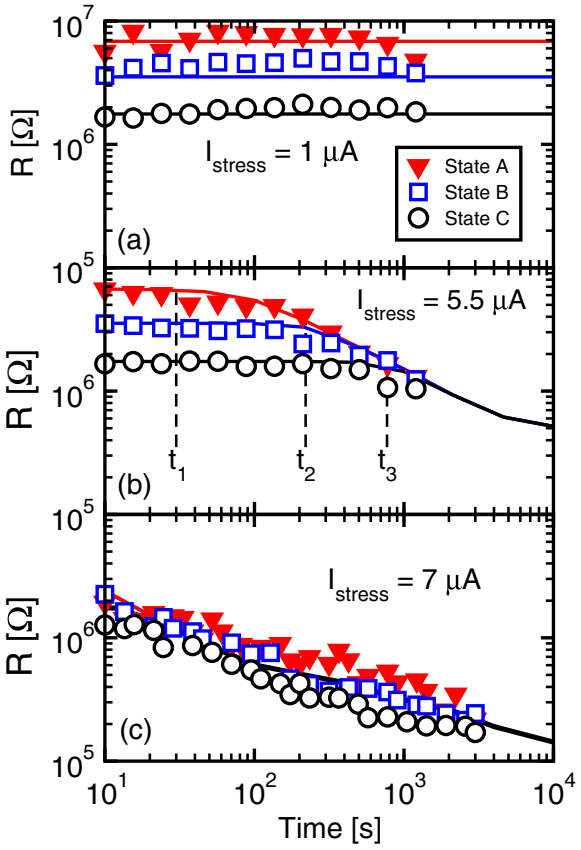

Fig. 14. Measured and calculated $R(t)$ for the 3 partial-set states in Fig. 13 under CCS at I_{stress} = 1 μA (a), 5.5 μA (b) and 7 μA (c). At any given I_{stress}, states at high R moves first, then the 3 states display the same behavior once they reach the same R.

process [6], [27], by considering the median R over 30 samples distribution.

To model crystallization in the read disturb regime we adopted a simplified approach, where the axial-symmetric filament concept is extended to the low current regime. The filament radius was chosen to match the voltage drop across the cell. The filament picture is consistent with the percolation behavior of conduction in the subthreshold regime [26], and with the PCM device being initially in a partial set state.

CCS data in Fig. 14 are reported for three different initial R of the partial set state, namely R = 8 MΩ (State A), 4 MΩ (State B) and 2 MΩ (State C). The time for the initial R decay decreases for increasing R, due to the higher voltage drop across the cell. However, as the time increases, CCS characteristics tend to merge into a single curve for any I_{stress}. This behavior can be understood by Fig. 15, showing the calculated temperature and crystalline fraction along the symmetry axis during CCS with I_{stress} = 5.5 μA, at increasing times t_1, t_2 and t_3 ($t_1 < t_2 < t_3$) as indicated in Fig. 14(b). The CCS experiments were not performed on the full reset state, since the relatively high currents needed to monitor R decay in a reasonable time were above the threshold switching point in the full reset state. However, the universal behavior highlighted in our work can be extended also to the reset state.

At first, the highest temperature is found in State A (a),

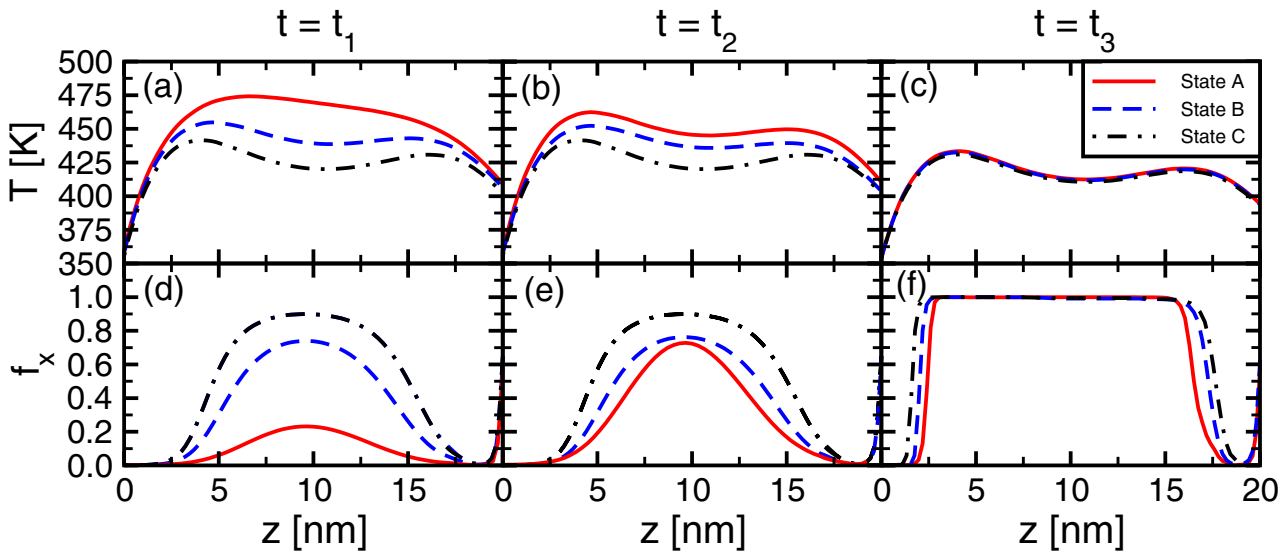

Fig. 15. Calculated temperature during CCS on three states with the same R of the states in Fig. 13, at 5.5 μA at increasing times $t_1 = 30$ ns (a), $t_2 = 200$ ns (b) and $t_3 = 800$ ns (c), and the calculated crystalline fraction f_x for the same times (d-f). The local temperature is initially higher for A (a) due to the lower crystalline phase content (d), therefore crystallization is faster in A in Fig. 14(b). At $t = t_2$, the temperature (b) and crystalline fraction (e) in A reach a similar profile as in B, thus causing a similar crystallization behavior of B and A. Due to the same self-limiting crystallization process, the three states show similar temperature (c) and phase composition (f) at $t = t_3$.

where the crystalline fraction is the lowest, thus Joule heating is higher (d) than in State B and State C. This leads to faster crystallization for State A, and at $t = t_2$ State A and State B tend to correspond in terms of phase temperature (b) and phase composition (e). At this point, the temperature is higher for State A and State B with respect to State C, resulting in faster crystallization in State A and State B compared to State C. Therefore, the temperature (c) and phase composition (f) of the three partial set states tend to overlap together at $t = t_3$, thus leading to the same resistance evolution for $t > 10^3$ s, as shown in Fig. 14(b). The disturb characteristic in Fig. 14(a) is still in the early stages of Fig. 15(a) and (d), where crystallization has yet to show up. On the other hand, the disturb characteristic in Fig. 14(c) already shows the convergence of the 3 curves due to the self limiting heating and crystallization process in Fig. 15. Fig. 16 summarizes the CCS for State A at increasing I_{stress}. The decay of resistance is faster at increasing I_{stress} due to increased Joule-heating in the amorphous dome. The crystallization times t_x extracted in correspondence of $R = 1$ MΩ for both data and calculations in Fig. 16 are reported in Fig. 6(b), highlighting the steep increase of crystallization time due to non-Arrhenius behavior below about 10 μA. The ability of our model of reproducing R decay in both set and read disturb regimes supports our initial hypothesis, where Joule-heating is the driving force for crystallization during pulse application.

V. Conclusions

This work presents an extensive characterization and modeling of pulse-induced crystallization in PCM devices under both the set and read disturb regimes. To this purpose, a new experimental technique is introduced to study low-current crystallization kinetics down to holding current, which allows

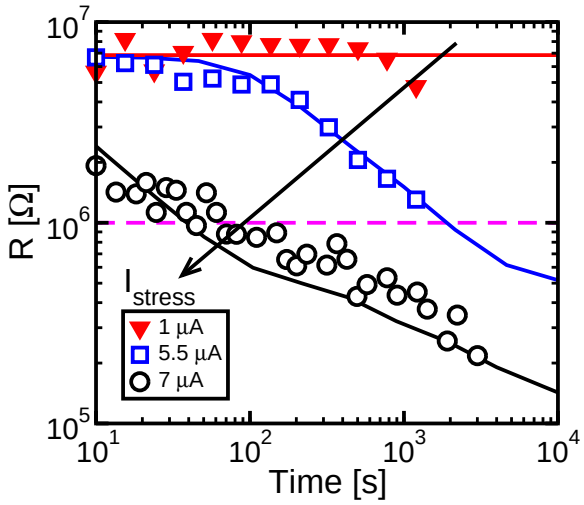

Fig. 16. Measured and calculated $R(t)$ at increasing I_{stress} for a partial-set state with initial $R = 8$ MΩ. The crystallization time t_x decreases at increasing I_{stress} due to stronger Joule-heating.

extending the range of measurable crystallization times. To describe crystallization in this wide time range, we developed a finite element model based on filamentary conduction in the amorphous phase after threshold switching and on thermally activated crystallization kinetics. The model is the applied to study disturb characteristics when the cells are operated in the subthreshold regime, allowing for accurate prediction of set and read disturb processes.

VI. Acknowledgements

The authors acknowledge Micron Technologies for providing experimental samples.

REFERENCES

[1] G. W. Burr, B. N. Kurdi, J. C. Scott, C. H. Lam, K. Gopalakrishnan, and R. S. Shenoy, "Overview of candidate device technologies for storage-class memory," *IBM J. Res. Develop.*, vol. 52, pp. 449–464, 2008.

[2] D. Loke, T. H. Lee, W. J. Wang, L. P. Shi, R. Zhao, Y.-C. Yeo, T.-C. Chong, and S. R. Elliott, "Breaking the speed limits of phase-change memory," *Science*, vol. 336, pp. 1566–1569, 2012.

[3] F. Xiong, A. D. Liao, D. Estrada, and E. Pop, "Low-power switching of phase-change materials with carbon nanotube electrodes," *Science*, vol. 332, pp. 568–570, 2011.

[4] G. Servalli, "A 45nm generation phase change memory technology," in *IEDM Tech. Dig.*, 2009, pp. 113–116.

[5] N. Ciocchini, M. Cassinerio, D. Fugazza, and D. Ielmini, "Evidence for non-Arrhenius kinetics of crystallization in phase change memory devices," *IEEE Trans. Electron Devices*, vol. 60, pp. 3767–3773, November 2013.

[6] A. Redaelli, D. Ielmini, U. Russo, and A. L. Lacaita, "Intrinsic data retention in nanoscaled PCMs – Part II: Statistical analysis and prediction of failure time," *IEEE Trans. Electron Devices*, vol. 53, pp. 3040–3046, 2006.

[7] S. H. Lee, M. S. Kim, G. S. Do, S. G. Kim, H. J. Lee, J. S. Sim, N. G. Park, S. B. Hong, Y. H. Jeon, K. S. Choi, H. C. Park, T. H. Kim, J. U. Lee, H. W. Kim, M. R. Choi, S. Y. Lee, Y. S. Kim, H. J. Kang, J. H. Kim, H. J. Kim, Y. S. Son, B. H. Lee, J. H. Choi, S. C. Kim, J. H. Lee, S. J. Hong, and S. W. Park, "Programming disturbance and cell scaling in phase change memory: For up to 16 nm based $4F^2$ cell," in *VLSI Tech. Dig.*, 2010, pp. 199–200.

[8] A. Pirovano, A. Redaelli, F. Pellizzer, F. Ottogalli, M. Tosi, D. Ielmini, A. L. Lacaita, and R. Bez, "Reliability study of phase change nonvolatile memories," *IEEE Trans. Device Mater. Reliab.*, vol. 4, pp. 422–427, 2004.

[9] D. Ielmini, A. Lacaita, A. Pirovano, F. Pellizzer, and R. Bez, "Analysis of phase distribution in phase-change nonvolatile memories," *IEEE Electron Device Lett.*, vol. 25, pp. 507–509, July 2004.

[10] A. Redaelli, M. Boniardi, A. Ghetti, U. Russo, C. Cupeta, S. Lavizzari, A. Pirovano, and G. Servalli, "Interface engineering for thermal disturb immune phase change memory technology," in *IEDM Tech. Dig.*, 2013, pp. 750–753.

[11] N. Ciocchini and D. Ielmini, "Modeling of crystallization kinetics in phase change memories for set and read disturb regimes," in *Proc. IRPS*, 2014, pp. 5E.1.1–5E.1.6.

[12] D. Ielmini, D. Mantegazza, and A. L. Lacaita, "Voltage-controlled relaxation oscillations in phase-change memory devices," *IEEE Electron Device Lett.*, vol. 29, pp. 568–570, 2008.

[13] D. Kau, S. Tang, I. V. Karpov, R. Dodge, B. Klehn, J. A. Kalb, J. Strand, A. Diaz, N. Leung, J. Wu, S. Lee, T. Langtry, K. Chang, C. Papagianni, J. Lee, J. Hirst, S. Erra, E. Flores, N. Righos, H. Castro, and G. Spadini, "A stackable cross point phase change memory," in *IEDM Tech. Dig*, 2009, pp. 617–620.

[14] S. Lavizzari, D. Ielmini, and A. L. Lacaita, "A new transient model for recovery and relaxation oscillations in phase change memories," *IEEE Trans. Electron Devices*, vol. 57, pp. 1838–1845, 2010.

[15] A. Fantini, V. Sousa, L. Perniola, E. Gourvest, J. C. Bastien, S. Maitrejean, S. Bragad, N. P. A. Bastard, B. Hyota, A. Roule, A. Persico, H. Feldis, C. Jahan, J. F. Nodin, D. Blachier, A. Toffoli, G. Reimbold, F. Fillot, F. Pierre, R. Annunziata, D. Benshael, P. Mazoyer, C. VallÃľe, T. Billon, J. Hazart, B. D. Salvo, and F. Boulanger, "N-doped GeTe as performance booster for embedded phase-change memories," in *IEDM Tech. Dig*, 2010, pp. 644–649.

[16] A. Faraclas, G. Bakan, L. Adnane, F. Dirisaglik, N. E. Williams, A. Gokirmak, and H. Silva, "Modeling of thermoelectric effects in phase change memory cells," *Electron Devices, IEEE Transactions on*, vol. 61, no. 2, pp. 372–378, 2014.

[17] A. Faraclas, N. Williams, A. Gokirmak, and H. Silva, "Modeling of set and reset operations of phase-change memory cells," *Electron Device Letters, IEEE*, vol. 32, no. 12, pp. 1737–1739, 2011.

[18] A. Cywar, J. Li, C. Lam, and H. Silva, "The impact of heater-recess and load matching in phase change memory mushroom cells," *Nanotechnology*, vol. 23, p. 225201, 2012.

[19] A. Faraclas, N. Williams, F. Dirisaglik, K. Cil, A. Gokirmak, and H. Silva, "Operation dynamics in phase-change memory cells and the role of access devices," *IEEE Computer Society Annual Symposium on VLSI*, pp. 78–83, 2012.

[20] G. Ruitenberg, A. K. Petford-Long, and R. C. Doole, "Determination of the isothermal nucleation and growth parameters for the crystallization of thin $Ge_2Sb_2Te_5$ films," *J. Appl. Phys.*, vol. 92, pp. 3116–3123, 2002.

[21] G. C. Sosso, G. Miceli, S. Caravati, F. Giberti, J. Behler, and M. Bernasconi, "Fast crystallization of the phase change compound GeTe by large- scale molecular dynamics simulations," *J. Phys. Chem. Lett.*, vol. 4, pp. 4241–4246, 2013.

[22] M. Cassinerio, N. Ciocchini, and D. Ielmini, "Evidence for electrically induced drift of threshold voltage in $Ge_2Sb_2Te_5$," *Appl. Phys. Lett.*, vol. 103, p. 023502, 2013.

[23] P. Fantini, M. Ferro, A. Calderoni, and S. Brazzelli, "Disorder enhancement due to structural relaxation in amorphous $Ge_2Sb_2Te_5$," *Appl. Phys. Lett.*, vol. 100, p. 213506, 2012.

[24] M. Boniardi and D. Ielmini, "Physical origin of the resistance drift in amorphous phase-change materials," *Appl. Phys. Lett.*, vol. 98, p. 243506, 2011.

[25] P. Fantini, M. Ferro, and A. Calderoni, "Field-accelerated structural relaxation in the amorphous state of phase change memory," *Appl. Phys. Lett.*, vol. 102, p. 253505, 2013.

[26] M. Rizzi, M. Ferro, P. Fantini, and D. Ielmini, "Energy landscape model of conduction and phase transition in phase change memories," *IEEE Trans. Electron Devices*, vol. 60, no. 11, pp. 3618–3624, 2013.

[27] U. Russo, D. Ielmini, A. Redaelli, and A. L. Lacaita, "Intrinsic data retention in nanoscaled PCMs – Part I: Monte Carlo model for crystallization and percolation," *IEEE Trans. Electron Devices*, vol. 53, pp. 3032–3039, 2006.